Title page

Effect of Bimodal Grain Size Distribution on Fatigue Properties of Ti-6Al-4V Alloy with Harmonic Structure under Four-point Bending

Shoichi KIKUCHI [a,*], Yosuke HAYAMI [b], Takayuki ISHIGURI [b], Benjamin GUENNEC [c], Akira UENO [c] , Mie OTA [c] and Kei AMEYAMA [c]

[a] Department of Mechanical Engineering, Graduate School of Engineering, Kobe University, 1-1 Rokkodai-cho, Nada-ku, Kobe, 657-8501, JAPAN

[b] Graduate School of Science and Engineering, Ritsumeikan University, 1-1-1 Noji-higashi, Kusatsu, Shiga, 525-8577, JAPAN

[c] Department of Mechanical Engineering, College of Science and Engineering, Ritsumeikan University, 1-1-1 Noji-higashi, Kusatsu, Shiga, 525-8577, JAPAN

*: Corresponding author

E-mail address: kikuchi@mech.kobe-u.ac.jp,

Phone: +81-78-803-6329, Fax: +81-78-803-6155

Abstract

Titanium alloy (Ti-6Al-4V) with a bimodal harmonic structure, which is defined as a coarse-grained structure surrounded by a network structure of fine grains, was fabricated using powder metallurgy to improve both the strength and ductility. The microstructure of the sintered compacts was characterized using electron backscattered diffraction (EBSD). The areal fraction of the fine-grained structure in the harmonic structure tended to increase with the milling time. Tensile tests and four-point bending fatigue tests at a stress ratio of 0.1 were performed in air at room temperature. The tensile strength, 0.2% proof stress and fatigue limit of Ti-6Al-4V alloy with harmonic structure tended to increase as the areal fraction of the fine-grained structure increased. In contrast, elongation decreased due to the formation of a high areal fraction of the fine-grained structure (79.0%), which resulted in a reduction of the fatigue life with a low cycle regime. Thus, titanium alloy with high strength, ductility and fatigue resistance can be formed by optimization of the milling conditions. Furthermore, the mechanism for fatigue fracture of the Ti-6Al-4V alloy with a harmonic structure is discussed with respect to fractography and crystallography. A fatigue crack was initiated from the α-facet of the coarse-grained structure in the harmonic structure.

Keywords

Fatigue; titanium alloy; grain refinement; powder metallurgy; fractography

Text, double-spaced

1. Introduction

The mechanical properties of metallic materials are influenced by their microstructure; therefore, grain-refinement processes are an effective means of improving the yield strength of metallic materials [1-3]. The titanium alloys highlighted in the present study have high strength requirements because these materials are used as biomaterials and mechanical components subjected to cyclic loading. However, a homogeneous fine-grained structure formed by severe plastic deformation generally leads to a decrease in the ductility of metallic materials [3-8] due to the initiation of plastic instability in the early stage. Therefore, various microstructural designs have been proposed to improve both the strength and ductility of these materials [4-16].

For example, Morita et al. [9] reported that the strength of Ti-6Al-4V alloy was improved by a short-time duplex heat treatment without a reduction in ductility. In particular, we have developed a harmonic structure design [12-19], which consists of a coarse-grained structure surrounded by a network structure of fine grains, using a powder metallurgy to improve both the strength and ductility of commercially pure titanium and Ti-6Al-4V alloy. The most significant difference between the harmonic structure, which can be formed by sintering mechanically-milled powders, and a conventional bimodal structure is that all of the fine-grained structures are interconnected in a continuous network. In the proposed microstructure design, the titanium-based harmonic structured materials exhibited higher

strength and elongation than their homogeneous counterparts [13-16] due to the preventation of stress and strain localization during the tensile tests.

In an attempt to achieve sufficient performance of titanium-based harmonic structured materials for practical applications in the engineering fields, we have examined the fatigue properties and the near-threshold fatigue crack propagation of Ti-6Al-4V alloy with harmonic structure [16,18,19]. It has been clarified that the crack path in Ti-6Al-4V alloy is influenced by the harmonic structure, which results in decreases of the threshold stress intensity range ΔK_{th}, effective threshold stress intensity range $\Delta K_{eff,th}$, and the closure stress intensity factor, K_{cl}. Furthermore, resistance to fatigue crack initiation can be changed by the presence of the fine-grained structure in the harmonic structure, so the fatigue properties of the harmonic structured material are dependent on their microstructure. The grain size distribution of titanium-based harmonic structured materials can be controlled by changing process parameters such as the number of passes during jet milling [13] and the mechanical milling time [17]; therefore, the effects of bimodal grain size distribution on the fatigue properties in harmonic structured Ti-6Al-4V alloy should be examined.

The purpose of the present study is to examine the fatigue properties of the harmonic structured Ti-6Al-4V alloy with a different bimodal grain size distribution under four-point bending, and to discuss the mechanism for fatigue fracture of the harmonic structured Ti-6Al-4V alloy with respect to the fractography and crystallography of the material.

2. Experimental procedures

2.1 Material and specimen preparation

The material used in the present study was Ti-6Al-4V alloy with a chemical composition (mass %) of Al 6.51, V 4.26, Fe 0.17, H 0.0023, N 0.003, O 0.18, C 0.01, and Ti marking up the balance. The powders (186 μm particle diameter) were produced using the plasma rotating electrode process (PREP) [20]. The PREP can be used to fabricate spherical particles that have negligible contamination with impurities such as oxygen or nitrogen gases. Mechanical milling of the Ti-6Al-4V powders was performed using a planetary ball mill (Fritch P-5) with a tungsten carbide vessel and SUJ2 steel balls (9.5 mm diameter) in an argon gas atmosphere at room temperature with a rotational speed of 200 rpm for 90 ks (MM90) or 360 ks (MM360). The ball-to-powder weight ratio was chosen to be 1.8:1 to form fine grains at the powder particle surfaces. The powders were subsequently consolidated by spark plasma sintering (SPS) at 1123 K for 1.8 ks under vacuum. The applied pressure was lower than 15 Pa and 50 MPa using 15 mm and 25 mm internal diameter graphite dies to produce the MM90 and MM360 specimens for tensile tests and fatigue tests, respectively. Sintered samples were also fabricated from the as-received initial powders for comparison (Untreated series). A total of three specimen types with different microstructures were prepared. To examine the effects of milling time on the grain size distribution of the sintered compacts, the microstructures were characterized using electron backscattered diffraction (EBSD) at an accelerating voltage of 20 kV.

2.2 Testing

The mechanical properties of the sintered compacts were evaluated using tensile tests. The tensile tests were conducted for the specimens with gauge dimensions of 3×1×1 mm^3 using a tensile testing apparatus (Shimadzu AGS-10kND) at a strain rate of 5.6×10^{-4} s^{-1}. Prior to testing, the specimens were polished to a mirror-finish using emery paper (#320 to #4000) and finally a SiO_2 suspension.

Four-point bending fatigue tests were conducted in an electrodynamic fatigue testing apparatus under stress ratio R of 0.1 using the mirror-finished specimens with dimensions of 18×3×1 mm^3 prepared from the 25 mm diameter sintered compacts. The sides of the specimen for the fatigue tests were also polished with emery paper (#500) to remove the electro-discharge machined layer. The frequency of stress cycling was 10 Hz, and the tests were conducted in the laboratory atmosphere. After testing, the fracture surfaces of the failed specimens were observed using scanning electron microscopy (SEM) and crack initiation sites were analyzed using EBSD.

3. Results and discussion

3.1 Microstructural characterization of sintered compacts

The microstructure of the sintered compacts was characterized before the fatigue tests were performed. Figure 1 shows grain boundary maps determined by EBSD analysis for (a) Untreated, (b) MM90 and (c) MM360 specimens, where the black lines represent

high-angle grain boundaries with misorientations greater than 15°. The Untreated specimen had a coarse acicular microstructure (Fig. 1(a)), whereas both the MM specimens contained two different microstructures: regions of fine equiaxed grains and regions with a coarse acicular microstructure (Figs. 1(b) and 1(c)). The regions of fine equiaxed grains formed a continuously connected network structure that surrounded the coarse acicular microstructure. This network structure is referred to as a harmonic structure.

Figure 2 shows the grain size distribution determined by EBSD analysis for the (a) Untreated, (b) MM90 and (c) MM360 specimens. In this study, fine grains are defined as grains less than 10 μm in size. The Untreated specimen had a majority of coarse grains larger than 40 μm, encompassing an area of more than 65.3% (Fig. 2(a)), and grains larger than 10 μm occupied almost 94.0% of the microstructure. Figure 2 also shows that the areal fraction of fine grains less than 10 μm was significantly increased by mechanical milling, at the expense of coarser grains (Figs. 2(b) and 2(c)). In particular, no coarse grains larger than 40 μm were observed in the MM360 series (Fig. 2(c)). Furthermore, both the MM specimens contained a wide grain size distribution, which could be considered as a bimodal microstructure that included regions of fine grains and regions with a coarse microstructure, as shown in Figs. 1(b) and 1(c).

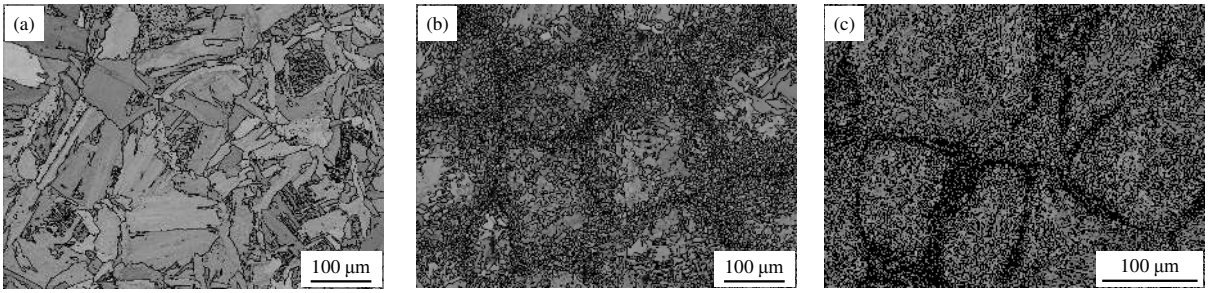

Fig.1 Grain boundary maps determined by EBSD analysis for the (a) Untreated, (b) MM90 and (c) MM360 specimens.

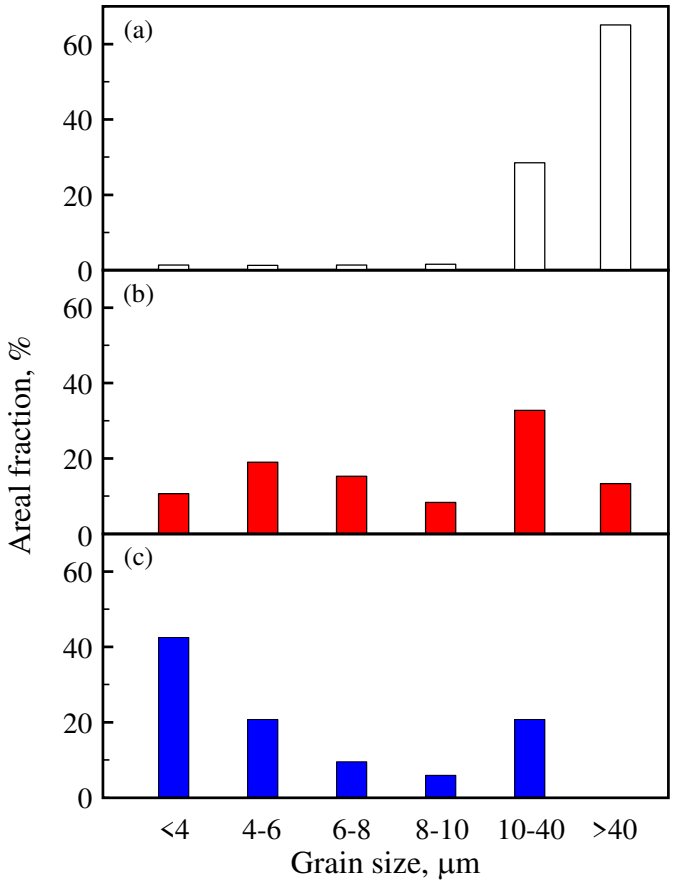

Fig.2 Grain size distribution determined by EBSD analysis for the (a) Untreated, (b) MM90 and (c) MM360 series.

Table 1 summarizes the average grain size of the sintered compacts with respect to the (a) entire microstructure, (b) fine-grained structure, (c) coarse-grained structure, and (d) the area of fine-grained microstructure. The average grain size of the sintered compacts

clearly tends to decrease with the milling time (Table 1(a)). This is because grain refinement occurs at the powder particle surfaces and the volume fraction of the fine-grained microstructure in the powder particles increases with the milling time due to an increase in the strain induced by mechanical milling, which results in a decrease of the average grain size in the fine-grained structure and an increase of the areal fraction of fine-grained structure in the sintered compacts (Table 1(b) and 1(d)). Our previous study [21] revealed that the severely deformed fine-grains microstructure consisted of nano-sized crystallites at the near-surface region of the mechanically milled powder by means of TEM observations. The grain size in the sintered compacts was larger than that in the mechanically milled powder, which indicates that grain growth of Ti-6Al-4V alloy occurred during the SPS. However, fine-grained structure was observed on the sintered compacts, as shown in Figs. 1(b) and (c); therefore, grain growth rate was a relatively low due to the formation of the high-angle grain boundaries on the surface of the mechanically milled powder. Furthermore, the average grain size in the coarse-grained structure also tended to decrease with the milling time (Table 1(c)), which implies that the microstructure at the center of powder particles also becomes fine during mechanical milling. Consequently, the grain size and the areal fraction of both the fine- and coarse-grained microstructures in Ti-6Al-4V alloy can be controlled by varying the milling conditions.

Table 1 Average grain size and areal fraction of the fine-grained structure in sintered compacts.

Milling time, ks	0	90	360
(a) Average grain size in entire microstructure, μm	10.8	5.2	3.1
(b) Average grain size in fine-grained structure, μm	4.6	4.6	2.9
(c) Average grain size in coarse-grained structure, μm	26.3	16.9	15.7
(d) Areal fraction of fine-grained structure, %	6.0	53.5	79.0

3.2 Evaluation of the effects of grain size distribution on the mechanical properties of sintered compacts

Figure 3 shows the strength (tensile strength and 0.2% proof stress) and the ductility (total elongation and uniform elongation) of the sintered compacts as a function of the areal fraction of the fine-grained structure and of the milling time. Both the tensile strength and 0.2% proof stress tended to increase with the milling time. The areal fraction of the fine-grained structure increased as the milling time increased, as shown in Table 1(d); therefore, the tensile strength and 0.2% proof stress increased with the areal fraction of the fine-grained structure. In contrast, both the total elongation and uniform elongation remained constant up to a milling time of 90 ks and then decreased. In particular, the total elongation was significantly decreased in the MM360 series, which has a 79.0% fine-grained structure.

This result indicates that the MM360 series exhibits lower ductility than the Untreated and MM90 series due to the high areal fraction of the fine-grained structure. However, uniform elongation was minimal with a decrease in the milling time compared to the total elongation. This is attributed to continuous work hardening due to the suppression of deformation localization by the network structure.

Consequently, the MM90 material, which has a fine-grained structure for over 53.5% of the area, achieved high strength and ductility.

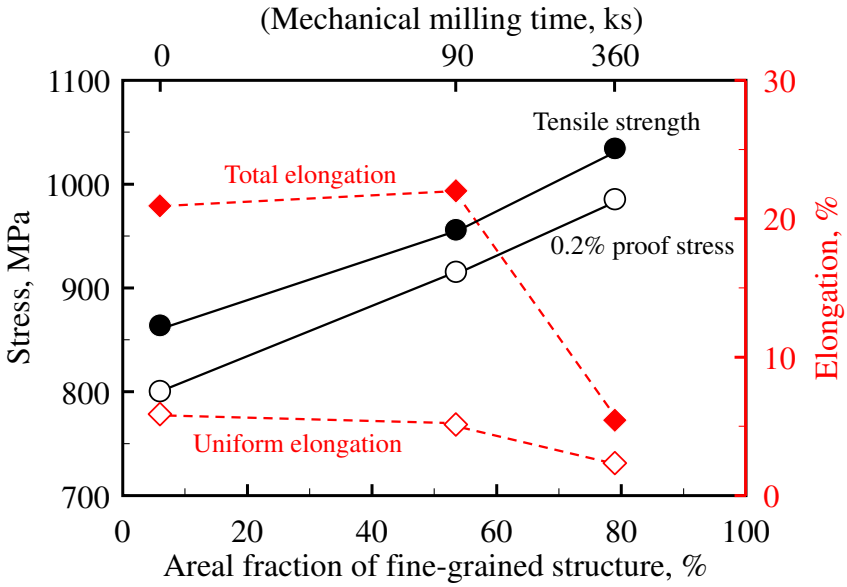

Fig. 3 Strength and elongation of the sintered compacts as a function of the areal fraction of the fine-grained structure and of the milling time.

3.3 Evaluation of the effects of grain size distribution on the four-point bending fatigue properties of sintered compacts

Figure 4 shows the results of four-point bending fatigue tests for the sintered

compacts; the maximum stress applied to the specimen surface σ_{max}, as function of the number of cycles to failure, N_f. Those plots with an arrow represent a run-out specimen without failure at $N = 10^7$ cycles, and each *S-N* curve is determined by accepting the *S-N* model with a fatigue limit in the JSMS standard regression models [22]. In the case of the Untreated series, the fatigue life had a large scatter, where one specimen did not fail at σ_{max} = 722 MPa at $N = 10^7$ cycles, while another failed at σ_{max} = 666 MPa. On the other hand, N_f for both the MM series tended to increase with a decrease in σ_{max}, with the exception of a MM360 specimen that failed at short fatigue life, as discussed in later. Figure 4 also shows that most of the MM360 series failed within a shorter fatigue life than the Untreated series, even though the fatigue life for the MM90 series was longer than that of the Untreated series. Figure 5 shows that fatigue limit σ_w, and the critical number of stress cycles to the fatigue limit N_w, as a function of the areal fraction of the fine-grained structure. The fatigue limit, which is defined based on the JSMS standard [22], tends to increase with the areal fraction of the fine-grained structure, in addition to the tensile strength and 0.2% proof stress, as shown in Fig. 3. In contrast, N_w remained constant up to a milling time of 90 ks and then significantly decreased. This trend was also observed for elongation, as shown in Fig. 3. The fatigue properties of Ti-6Al-4V alloy with harmonic structure were confirmed to be influenced by the grain size distribution, and the MM90 specimens exhibited superior four-point bending fatigue properties.

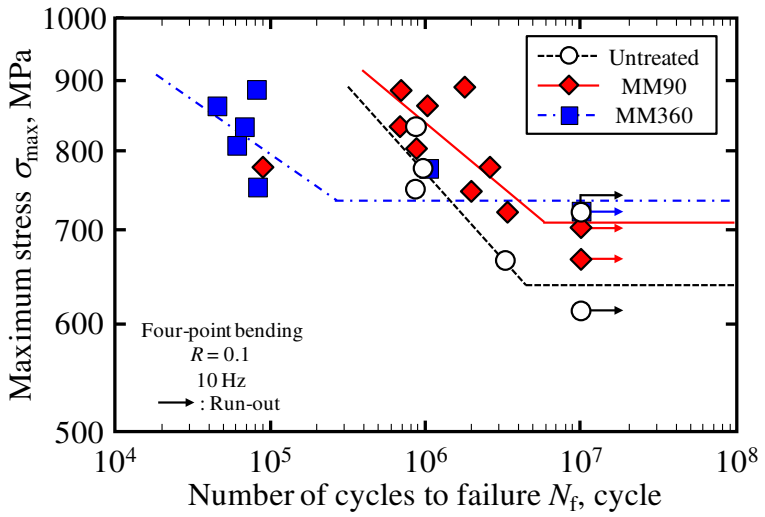

Fig. 4 Results of four-point bending fatigue tests; the maximum stress σ_{max}, as function of the number of cycles to failure, N_f.

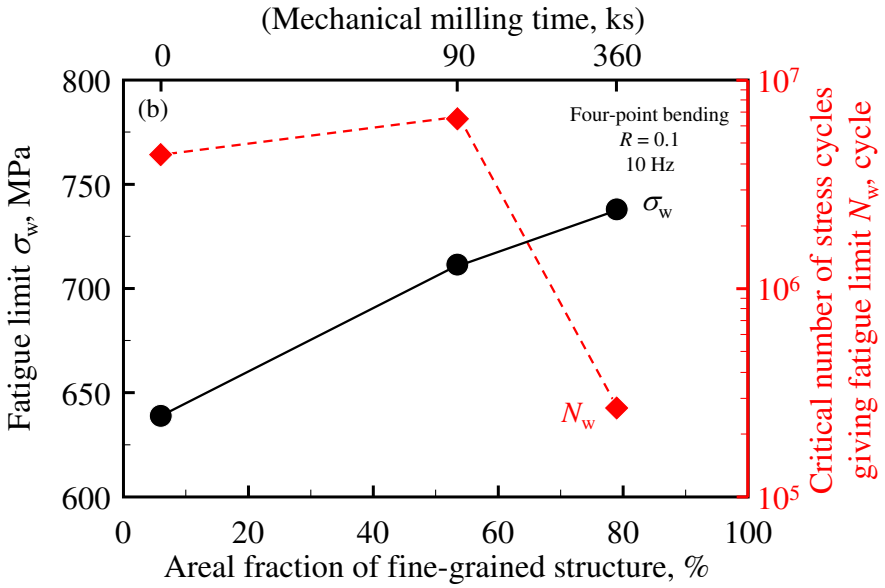

Fig. 5 Fatigue limit σ_w, and critical number of stress cycles to the fatigue limit N_w, as function of the areal fraction of the fine-grained structure.

To examine the effects of grain size distribution on the fatigue properties of Ti-6Al-4V alloy in more detail, σ_{max} was normalized according to the tensile strength, σ_{TS}.

Figure 6 shows the relationship between the normalized maximum stress σ_{max}/σ_{TS}, and N_f. The fatigue life of every specimen tended to decrease with a decrease in σ_{max}/σ_{TS} and the data for the Untreated and MM90 series were almost within the same band. In contrast, the MM360 series had a lower fatigue life, and the fatigue limit normalized according to the tensile strength σ_w/σ_{TS} (0.71), was lower than those of the Untreated and MM90 series (0.74). These results indicate that the fatigue properties of Ti-6Al-4V alloy are not determined by only the tensile strength but also by the ductility. Therefore, the MM360 series with low ductility exhibited low N_w because the fatigue properties within the low cycle regime are generally influenced by the ductility.

Consequently, titanium alloy with high strength, ductility and fatigue resistance can be formed by optimizing the milling conditions.

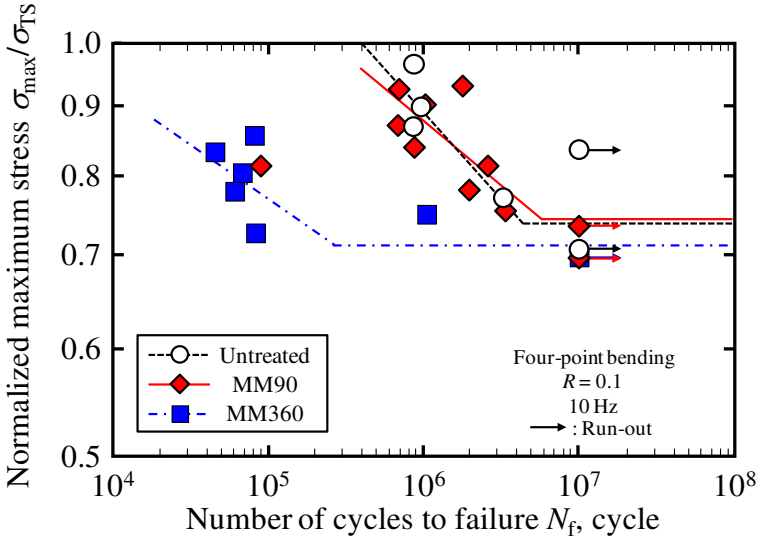

Fig. 6 Results of four-point bending fatigue tests; the maximum stress normalized according to the tensile strength σ_{max}/σ_{TS}, as a function of the number of cycles to failure, N_f.

3.4 Fractography

To clarify the mechanism for the fatigue fracture of the Ti-6Al-4V alloy with a harmonic structure, the fracture surfaces of the failed specimens were observed using SEM. Figure 7 shows the typical features of both fracture surfaces observed at various magnifications for the MM90 series that failed at a maximum stress of 722 MPa with a long fatigue life of $N_f = 3.4\times10^6$. The tensile stress was applied to the upper surfaces shown in the micrographs. Macroscopic observation revealed that only one fatigue crack was present near the specimen surface, which propagated gradually across the cross-section of the specimen. The fracture surface was divided into two regions by a clear boundary. In the higher magnification micrographs, no defects were observed on the fracture surfaces of the MM90 specimen that failed within the long fatigue life; however, characteristic facets with sizes larger than 10 μm were clearly observed, as indicated by the dotted lines.

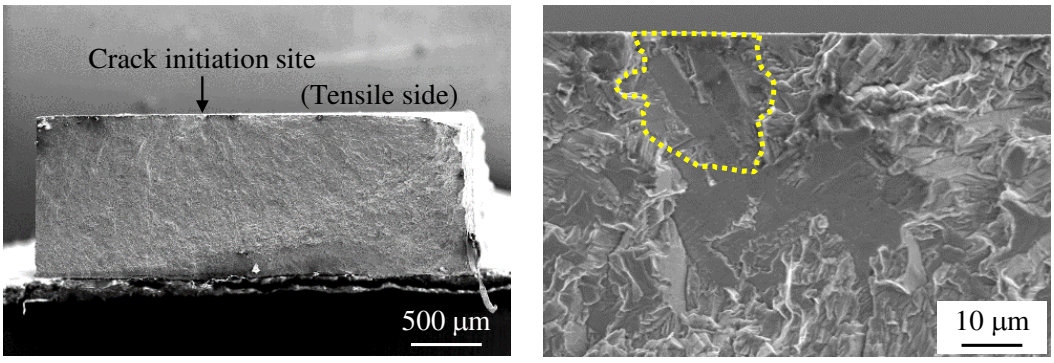

(a) Fracture surface 1

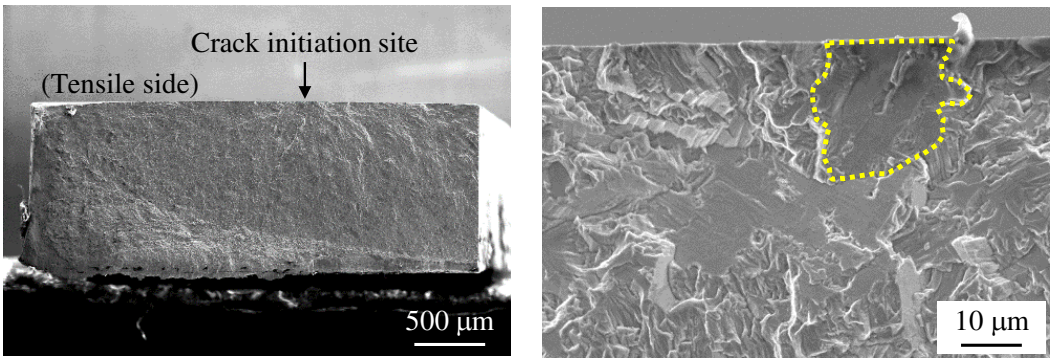

(b) Fracture surface 2

Fig. 7 Typical fracture surface features of the MM90 series failed at long fatigue life (σ_{max} = 722 MPa, $N_f = 3.4\times10^6$).

To clarify the microstructure near the crack initiation site, EBSD analysis was conducted for the facets observed on the fracture surfaces of the MM90 specimen that failed within the long fatigue life. Therefore, three-dimensional fracture surfaces were produced using MeX software (Alicona) for 3D-fracture surface reconstruction to calculate the angle of the fracture surfaces. Figure 8 shows plan views of both fracture surfaces of the MM90 series, as shown in Fig. 7. The analyzed positions and directions are shown in each micrograph. A normalized vector of the triangular plane CDE was estimated by performing profile analysis for the facet on fracture surface 2. Figures 9 and 10 show profile curves for fracture surfaces 1 and 2 of the MM90 series, respectively. The relationship between the height based on the lowest point within the analysis area and the distance from point A or point C are shown. The inclination angle of the facet observed on fracture surface 1 was 12.9°, and those for fracture surface 2 were 26.4° for CD and 23.2° for CE. Therefore, fatigue failure would occur at the

slip plane with a weak microstructural orientation.

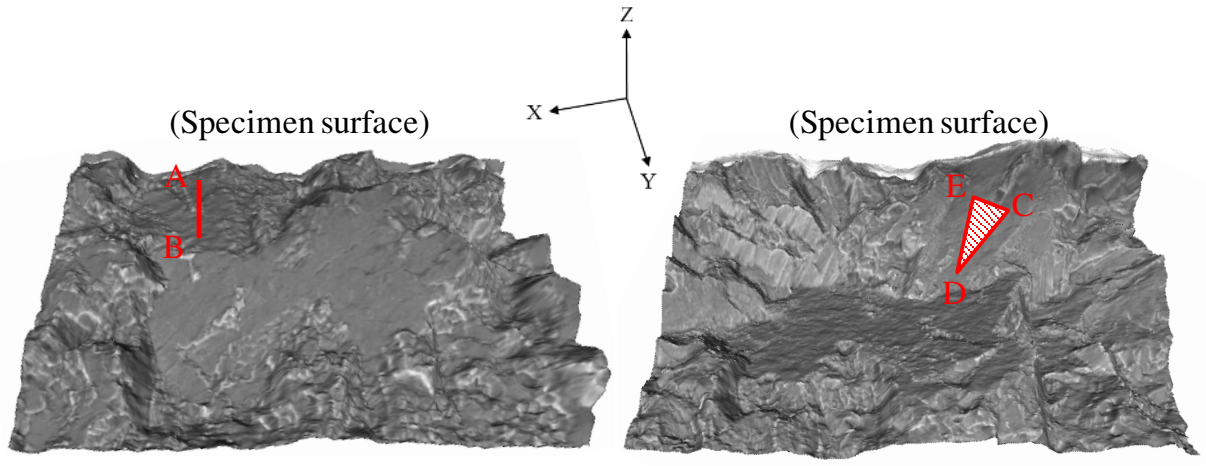

(a) Fracture surface 1 (b) Fracture surface 2

Fig. 8 Plan views of the fracture surfaces of the MM90 series failed at σ_{max} = 722 MPa, N_f = 3.4×10^6.

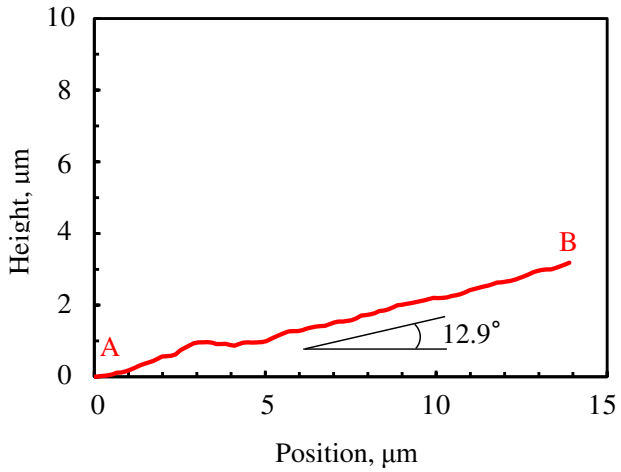

Fig. 9 Profile curve for the facet observed in fracture surface 1 of the MM90 series failed at σ_{max} = 722 MPa, $N_f = 3.4\times10^6$.

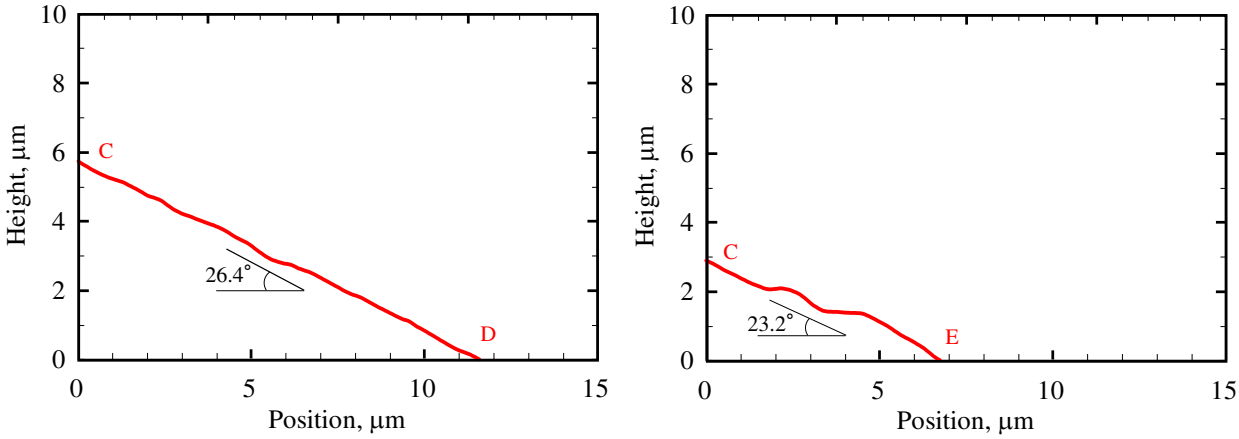

(a) Through points C and D (b) Through points C and E

Fig. 10 Profile curves for the facet observed in fracture surface 2 of the MM90 series failed at σ_{max} = 722 MPa, $N_f = 3.4\times10^6$.

After rotation on the XY plane and tilting on the XZ plane based on the results of profile analysis, EBSD analysis could be conducted for the fracture surfaces. Figure 11 shows SEM micrographs of the analysis areas and inverse pole figure (IPF) maps obtained using EBSD for both the fracture surfaces near the crack initiation site. The facets at the crack initiation sites of both fracture surfaces were α-phase and had the same crystal orientation with grain sizes of ca. 15 μm. This result indicates that a fatigue crack is initiated at the α-facet of the coarse-grained structure in the harmonic structure. Other researchers [23,24] have also reported that Ti-6Al-4V alloy fails from transgranular cracking of an α grain. Therefore, a relatively coarse α-microstructure is the predominant crack initiation site in Ti-6Al-4V alloy with a harmonic structure during fatigue tests.

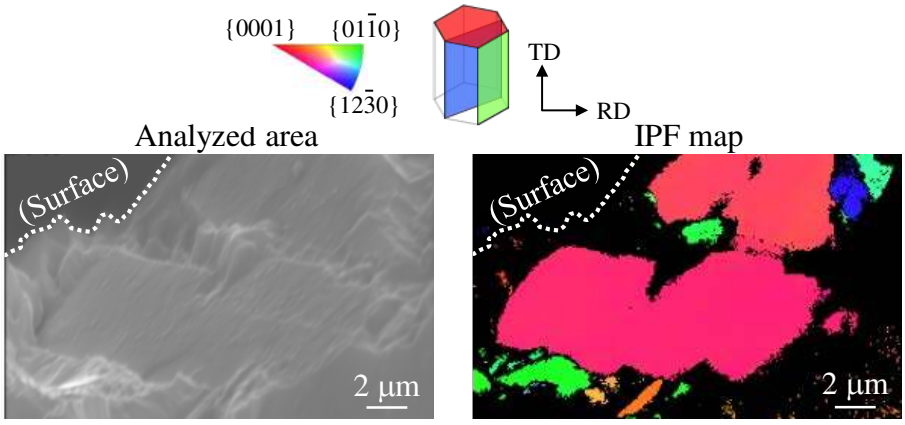

(a) Fracture surface 1

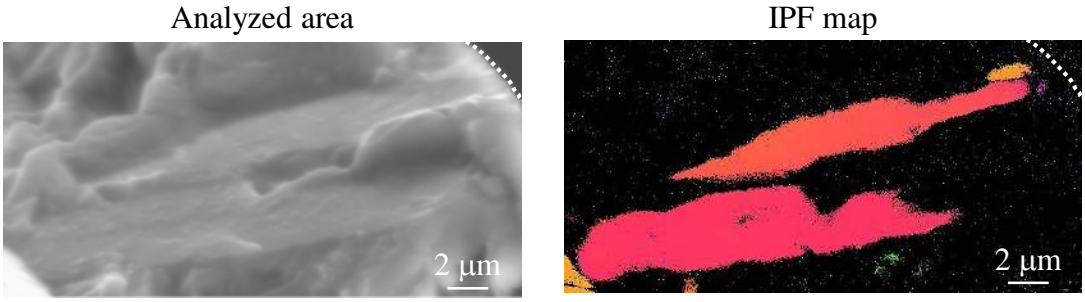

(b) Fracture surface 2

Fig. 11 SEM micrographs and IPF maps obtained by EBSD analysis for the facet observed in the fracture surfaces of the MM90 series failed at σ_{max} = 722 MPa, N_f = 3.4×10^6.

However, one MM90 specimen failed with a short fatigue life. Figure 12 shows the typical features of both fracture surfaces for the MM90 series that failed at a maximum stress of 778 MPa with a short fatigue life of N_f = 9.0×10^4. In this case, a coarse microstructure, which is indicated by the dotted lines in Fig. 12, was observed at the crack initiation site. Therefore, the coarse microstructure acted as a crack starter, and resulted in a reduction of the fatigue life.

Thus, it was confirmed that the fatigue properties of the titanium-based harmonic structured materials are influenced by their microstructure.

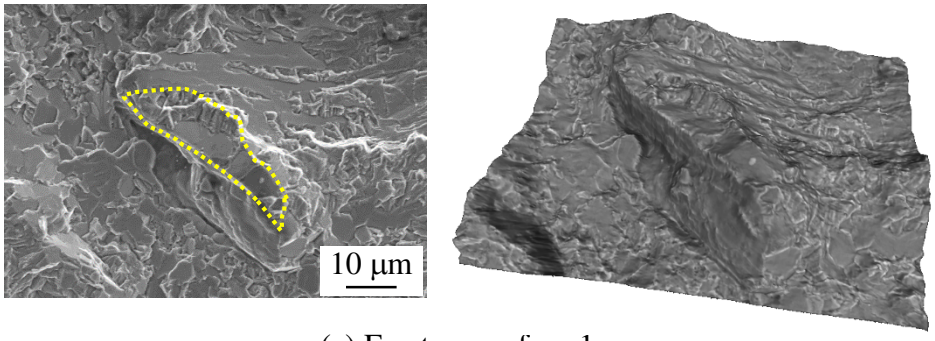

(a) Fracture surface 1

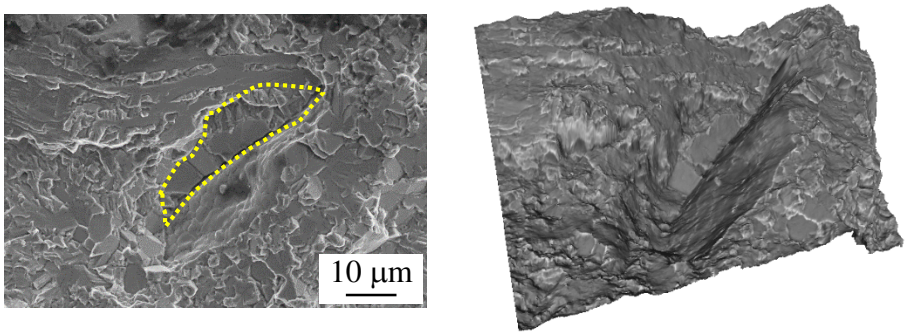

(b) Fracture surface 2

Fig. 12 Typical fracture surface features of the MM90 series failed at short fatigue life (σ_{max} = 778 MPa, $N_f = 9.0\times10^4$).

4. Conclusions

The effect of harmonic structure with a bimodal grain size distribution on the fatigue properties in titanium alloy (Ti-6Al-4V) under four-point bending was investigated, and the mechanism for fatigue fracture was discussed with respect to the fractography and crystallography. The main conclusions obtained in this study are summarized as follows:

1. The areal fraction of the fine-grained structure in the harmonic structure increases with the milling time.

2. Tensile strength, 0.2% proof stress and fatigue limit under four-point bending in Ti-6Al-4V alloy with harmonic structure tend to increase as the areal fraction of the fine-grained structure increases, whereas the elongation and fatigue life are low with a high areal fraction (79.0%) of the fine-grained structure.

3. The mechanical properties and fatigue properties of titanium alloy can be controlled by varying the milling conditions. In the present study, the sintered compact has a bimodal harmonic structure with a network structure of fine grains over 53.5% of the area, which leads to high strength, ductility and fatigue resistance.

4. A fatigue crack is initiated at an α-facet of the coarse-grained structure in the harmonic structured Ti-6Al-4V alloy during fatigue tests.

Acknowledgement

This work was partially supported by a KAKENHI Grant-in-Aid (No.15K05677) from the Japan Society for the Promotion of Science (JSPS). The authors would also like to thank Hosokawa Powder Technology Foundation and The Hattori Hokokai Foundation for financial support.

List of references

[1] E.O. Hall, Proc. Phys. Soc. B 64 (1951) 273.

[2] N.J. Petch, J. Iron and Steel Inst. 174 (1953) 25.

[3] N. Tsuji, Y. Ito, Y. Saito, Y. Minamoto. Scr. Mater. 47 (2002) 893.

[4] E. Ma, Scr. Mater. 49 (2003) 663.

[5] D. Terada, M. Inoue, H. Kitahara, N. Tsuji, Mater. Trans. 49 (2008) 41.

[6] T.H. Fang, W.L. Li, N.R. Tao, K.Lu, Science 331 (2011) 1587.

[7] N. Tsuji, N. Kamikawa, R. Ueji, N. Takata, H. Koyama, D. Terada, ISIJ Int. 48 (2008) 1114.

[8] Y. Wang, M. Chen, F. Zhou, E. Ma, Nature 419 (2002) 912.

[9] T. Morita, K. Hatsuoka, T. Iizuka, K. Kawasaki, Mater. Trans. 46 (2005) 1681.

[10] J.S. Peter, P.F. David, J. Bertalan, H. Jelena, U. Tamas, Metall. Mater. Trans. A 46 (2015) 1948.

[11] W. Witkin, Z. Lee, R. Rodriguez, S. Nutt, E. Lavernia, Scr. Mater. 49 (2003) 297.

[12] T. Sekiguchi, K. Ono, H. Fujiwara, K. Ameyama, Mater. Trans. 51 (2010) 39.

[13] M. Ota, S.K. Vajpai, R. Imao, K. Kurokawa, K. Ameyama, Mater. Trans. 56 (2015) 154.

[14] H. Fujiwara, T. Sekiguchi, K. Ameyama, Int. J. Mater. Res. 100 (2009) 796.

[15] S.K. Vajpai, M. Ota, T. Watanabe, R. Maeda, T. Sekiguchi, T. Kusaka, K. Ameyama, Metall. Mater. Trans. A. 46 (2015) 903.

[16] S. Kikuchi, K. Takemura, Y. Hayami, A. Ueno, K. Ameyama, J. Soc. Mater. Sci., Jpn. 64 (2015) 880.

[17] S. Kikuchi, Y. Nakamura, A. Ueno, K. Ameyama, Mater. Trans. 56 (2015) 1807.

[18] S. Kikuchi, T. Imai, H. Kubozono, Y. Nakai, A. Ueno, K. Ameyama, Fract. Struct. Int.

34 (2015) 261.

[19] S. Kikuchi, T. Imai, H. Kubonozo, Y. Nakai, M. Ota, A. Ueno, K. Ameyama, Int. J. Fatigue 92 (2016) 616.

[20] M. Tokizane, K. Isonishi, J. Jpn. Soc. Powder Metal. 39 (1992) 1137.

[21] S. K. Vajpai, M. Ota, Z. Zhang and K. Ameyama, Mater. Res. Lett. 4 (2016) 191-197.

[22] JSMS Committees on Fatigue of Materials and Reliability Engineering, Standard Regression Method of S-N Curves, The Society of Materials Science, Japan, (2008).

[23] R.K. Nalla, B.L. Boyce, J.P. Campbell, J.O. Peters, R.O. Ritchie, Metall. Mater. Trans. A 33 (2002) 899.

[24] H. Oguma, T. Nakamura, Scr. Mater. 63 (2010) 32.

List of table and figure captions

Table 1 Average grain size and areal fraction of the fine-grained structure in sintered compacts.

Fig. 1. Grain boundary maps determined by EBSD analysis for the (a) Untreated, (b) MM90 and (c) MM360 series.

Fig. 2. Grain size distribution determined by EBSD analysis for the (a) Untreated, (b) MM90 and (c) MM360 series.

Fig. 3. Strength and elongation of the sintered compacts as a function of the areal fraction of

the fine-grained structure and of the milling time.

Fig. 4. Results of four-point bending fatigue tests; the maximum stress σ_{max}, as function of the number of cycles to failure, N_f.

Fig. 5. Fatigue limit σ_w, and critical number of stress cycles to the fatigue limit N_w, as function of the areal fraction of the fine-grained structure.

Fig. 6. Results of four-point bending fatigue tests; the maximum stress normalized according to the tensile strength σ_{max}/σ_{TS}, as a function of the number of cycles to failure, N_f.

Fig. 7. Typical fracture surface features of the MM90 series failed at long fatigue life (σ_{max} = 722 MPa, $N_f = 3.4\times10^6$).

Fig. 8. Plan views of the fracture surfaces of the MM90 series failed at σ_{max} = 722 MPa, N_f = 3.4×10^6.

Fig. 9. Profile curve for the facet observed in fracture surface 1 of the MM90 series failed at σ_{max} = 722 MPa, $N_f = 3.4\times10^6$.

Fig. 10. Profile curves for the facet observed in fracture surface 2 of the MM90 series failed at σ_{max} = 722 MPa, $N_f = 3.4\times10^6$.

Fig. 11. SEM micrographs and IPF maps obtained by EBSD analysis for the facet observed in the fracture surfaces of the MM90 series failed at σ_{max} = 722 MPa, $N_f = 3.4\times10^6$.

Fig. 12. Typical fracture surface features of the MM90 series failed at short fatigue life (σ_{max} = 778 MPa, $N_f = 9.0 \times 10^4$).